Talanta 164 (2017) 330–340

Contents lists available at ScienceDirect

Talanta

journal homepage: www.elsevier.com/locate/talanta

Calibration-free quantitative analysis of elemental ratios in intermetallic nanoalloys and nanocomposites using Laser Induced Breakdown Spectroscopy (LIBS)

Seyyed Ali Davari[a,c], Sheng Hu[b,c], Dibyendu Mukherjee[a,c,*]

[a] Department of Mechanical, Aerospace, & Biomedical Engineering, University of Tennessee, Knoxville, TN 37996, USA
[b] Department of Chemical & Biomolecular Engineering, University of Tennessee, Knoxville, TN 37996, USA
[c] Nano-BioMaterials Laboratory for Energy, Energetics & Environment (nbml-E3), University of Tennessee, Knoxville, TN 37996, USA

ARTICLE INFO

Keywords:
Laser Induced Breakdown Spectroscopy (LIBS)
Intermetallic nanoalloys
Nanocomposites
Calibration-free
Quantitative analysis

ABSTRACT

Intermetallic nanoalloys (NAs) and nanocomposites (NCs) have increasingly gained prominence as efficient catalytic materials in electrochemical energy conversion and storage systems. But their morphology and chemical compositions play critical role in tuning their catalytic activities, and precious metal contents. While advanced microscopy techniques facilitate morphological characterizations, traditional chemical characterizations are either qualitative or extremely involved. In this study, we apply Laser Induced Breakdown Spectroscopy (LIBS) for quantitative compositional analysis of NAs and NCs synthesized with varied elemental ratios by our in-house built pulsed laser ablation technique. Specifically, elemental ratios of binary PtNi, PdCo (NAs) and PtCo (NCs) of different compositions are determined from LIBS measurements employing an internal calibration scheme using the bulk matrix species as internal standards. Morphology and qualitative elemental compositions of the aforesaid NAs and NCs are confirmed from Transmission Electron Microscopy (TEM) images and Energy Dispersive X-ray Spectroscopy (EDX) measurements. LIBS experiments are carried out in ambient conditions with the NA and NC samples drop cast on silicon wafers after centrifugation to increase their concentrations. The technique does not call for cumbersome sample preparations including acid digestions and external calibration standards commonly required in Inductively Coupled Plasma-Optical Emission Spectroscopy (ICP-OES) techniques. Yet the quantitative LIBS results are in good agreement with the results from ICP-OES measurements. Our results indicate the feasibility of using LIBS in future for rapid and in-situ quantitative chemical characterizations of wide classes of synthesized NAs and NCs.

1. Introduction

A critical bottleneck in the research and development of state-of-the-art electrochemical energy conversion and storage systems (including fuel cells and metal–air batteries) remains in the design of intermetallic nanoalloys (NAs) and nanocomposites (NCs) as efficient catalysts – the main goal being the replacement of precious metals (Pt, Au, Pd etc.) with cheaper transition metal oxides. Specifically, due to the unique physicochemical, structural and electronic characteristics, Pt/Pd-M (M stands for transition metals such as Co, Ni, Fe, Cu, etc.) NAs are regarded as highly promising electrocatalysts for oxygen reduction reaction (ORR) [3–6] and methanol/ethanol/formic acid oxidation reaction [7–9] in fuel cell applications. On another hand, NCs of transitional metal oxides, metal/intermetallic nanoparticles (NPs) in metal oxide matrices (including perovskites) are known to exhibit outstanding bifunctional activities for both ORR and oxygen evolution reactions (OER) [10–13]. However, the critical challenge remains in tailoring the elemental compositions of these NAs and NCs in an effort to tune their atomic lattice properties and in turn, their interfacial catalytic activities as well as precious metal loadings [14–17]. Thus, facile, efficient and, yet accurate chemical characterizations of a wide class of NAs and NCs become imperative for robust and rapid screening of superior catalysts.

Inductively Coupled Plasma Optical Emission Spectroscopy (ICP-OES), and X-ray photoelectron spectroscopy (XPS) have been the conventional analytical techniques of choice for chemical composition characterizations. In spite of the well-established analytical capabilities of ICP-OES and XPS due to the robust instrumentation development and accuracy, they have their own pitfalls in terms of experimental protocols. In the case of ICP-OES, considerable sample preparations

* Corresponding author at: Department of Mechanical, Aerospace, & Biomedical Engineering, University of Tennessee, Knoxville, TN 37996, USA.
E-mail address: dmukherj@utk.edu (D. Mukherjee).

http://dx.doi.org/10.1016/j.talanta.2016.11.031
Received 5 October 2016; Received in revised form 16 November 2016; Accepted 16 November 2016
Available online 23 November 2016

including external calibration standard requirements and rigorous acid digestions for many samples (including intermetallic NPs) prove to be highly problematic and time consuming [18–20]. Besides, many strong acids required for the sample digestions prove to be hazardous and incompatible with the instruments.

Laser Induced Breakdown Spectroscopy (LIBS) is a relatively non-destructive spectrochemical characterization technique, which can address the aforementioned issues in a facile, yet effective manner. Typically, LIBS involves the collection and processing of optical emissions emanating from a high-irradiance pulsed laser tightly focused to generate a high temperature, high pressure micro-plasma containing the analyte of interest [21]. These emissions (ionic, atomic and molecular), collected as spectral signatures, can reveal the constituents and properties of the plasma and hence, the sample. The relatively simple set-up, and minimal sample preparations for LIBS have drawn the attention of analytical researchers in recent years [22]. Moreover, the fast operation and easy data collection of LIBS make it an ideal analytical tool for in-situ studies [23].

In the past, LIBS has found a vast amount of applications in diverse spectral, and elemental studies ranging from combustion [24–26], and environmental/bio-hazard analysis [27–31], to forensics [32], explosives detection [33–35], pharmaceutical [36,37], and biomedical [38,39] applications. Specifically, LIBS has been used for elemental analysis in bulk metallic alloys and composites include bulk steel sample analysis using single and double pulsed lasers [40], and identification of aluminum impurities in zinc-based alloys [41], both of which involve the use of calibration standards. Additionally, analytical measurements combining LIBS and laser-induced fluorescence [42] have been used to establish low detection limits for cobalt in low-alloy steels. In spite of the extensive use of LIBS on bulk alloy analysis, there appears to be a noticeable dearth in its extension toward quantitative analysis of intermetallic NPs, including NAs and NCs. Recent years have seen a growing interest in the use of LIBS for detailed nanoparticle characterizations that include the exhaustive research by Hahn and his co-workers in the past on the sizing and elemental analysis of aerosolized metal/metal oxide NPs [43–45]. Such works have led to continued efforts on the application of LIBS for detecting impurities in iron oxide nano-powders/NCs for both industrial and biomedical applications [46,47], as well as in identifying volume fraction of flame synthesized titania NPs using phase-selective LIBS [48]. More recently, LIBS was also used in distinguishing nano-sized carbon materials based on molecular emissions from different graphitic lattices [49]. But, only a handful of works have employed LIBS for elemental analysis of complex intermetallic NPs. These include the in-situ confirmation of CuAg NP synthesis during laser ablation synthesis [50], and detection of Ytterbium (Yb) in cobalt antimony ($CoSb_3$) skutterudite voids [51]. While the aforesaid studies carried out some of the foremost spectrochemical characterizations of NPs and nanostructured materials, they have been largely limited to qualitative studies, or at the most, quantitative analysis based on external calibration standards. To this end, Mukherjee et al. [23] had carried out one of the formative studies in developing the calibration-free quantitative LIBS methodology to measure the extent of oxidation on Al nanoparticles. This methodology was later extended and verified for detailed quantitative LIBS characterizations of carbonaceous aerosols and aerosolized drugs [29,36]. To the best of our knowledge, no studies till date have successfully employed LIBS for quantitative elemental analysis of intermetallic NPs that can provide new directions toward future rapid and facile analytical techniques for in-situ chemical characterizations of complex heterogeneous nanomaterials during their large scale synthesis.

We address the aforesaid lapse in the application of LIBS toward rapid and high accuracy elemental characterizations of intermetallic NPs through our current work. It needs to be brought to attention that various calibration-free LIBS techniques have been developed in the past [52–54]. But the current study is specifically built on the earlier studies of Mukherjee et al. [23] to employ the calibration-free quantitative LIBS toward rapid and facile analysis of compositional variations in complex intermetallic NAs/NCs. Specifically, we focus on the elemental composition analysis of PdCo and PtNi NAs, and PtCo NCs synthesized via our recently developed Laser Ablation Synthesis in Solution-Galvanic Replacement Reaction (LASiS-GRR) technique as part of our ongoing research efforts on directed design of intermetallic nanomaterials with low precious metal loadings as efficient ORR electrocatalysts [6,10]. The accuracy of our results from the LIBS measurements will be verified by comparing against the corresponding results from ICP-OES analyses.

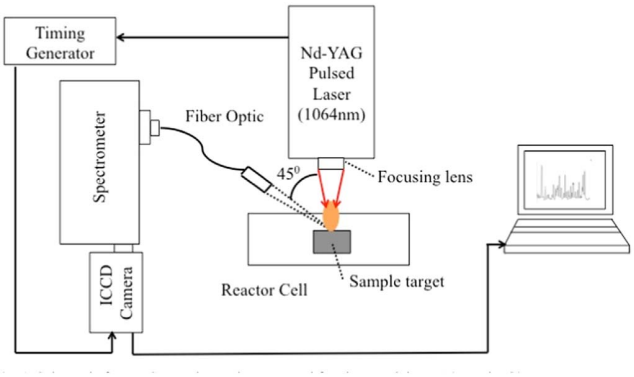

Fig. 1. Schematic for LIBS experimental set-up used for characterizing NA's, and NC's.

2. Experimental details

2.1. Experimental set-up

The experimental set-up is illustrated in Fig. 1. The laser-induced plasma is generated with a Q-switched Nd-YAG laser of nominal wavelength 1064 nm operating at 200 mJ/pulse, and a pulse width of 8 ns (Make: Insight Model: 122551-R). As seen in Fig. 1, the laser is focused with a 25 mm diameter fused silica lens (focal length=35 mm) that generates ~10–15 GW/cm^2 flux at the focal point on the target surface. The resulting high-energy plasma plume produces a high temperature that can reach up to ~30,000 K. The spot size on the sample is set to 75 μm diameter, which creates a plasma volume with size 1–2 mm^3 approximately. Due to the thin film of deposition, one laser shot per spot is collected. But, in order to improve the statistical average of the signal intensity for each analyte of interest, spectral data over approximately 100–150 spots are collected.

The plasma emission is collected with a fiber optic port carrying a collimation-focusing lens pair and placed at 45 degree collection angle (see Fig. 1), which yields the optimum intensity from the plasma volume. The focused light collected via a fiber optic cable is transmitted to a Czerny-Turner spectrometer (Make: Andor Technology; Model: Shamrock - SR-303i-A) with 1200 grooves/mm grating (resolution of 0.1 nm at 500 nm), and a nominal dispersion of 2.58 nm/mm. The slit width is fixed at 100 μm for all experiments carried out here in order to have the optimum spectral line intensity and resolution. A time-gated intensified charge-coupled device (ICCD) detector array (1024×1024 CCD) (Make: Andor Technology; Model: DH334T-18U-E3) detects the spectral lines at the spectrometer exit focal plane. The time gating is synchronized with the laser Q-switch through an in-built timing generator in the ICCD camera set-up.

2.2. Synthesis of NAs and NCs

Co and Ni pellets were provided from Kurt J. Lesker (99.95% purity, 1/4″ diameter×1/4″ height). K_2PtCl_4 (> 99.9%), Na_2PdCl_4 (> 99.9%) and HCl (37%) samples were purchased from Sigma-Aldrich.

All NA and NC samples for the present study were synthesized using our recently developed LASiS-GRR technique and described elsewhere [6,10,55]. In specific, for the synthesis of PtCo/CoO_x NCs, Co target was ablated by the pulsed laser in K_2PtCl_4 solutions with different concentrations of 25, 60, 120 mg/l, with the resultant samples marked as PtCo1, PtCo2 and PtCo3 respectively; For the preparation of PtNi and PdCo NAs, K_2PtCl_4 (250 mg/l) and Na_2PdCl_4 (125 mg/l) were used as the salt solutions, while Ni and Co were used as the targets separately. For all NA synthesis, any excess metal oxides were removed by subsequent acid-wash with HCl (pH2) solution as described in our earlier work [6]. Finally, the precipitates from centrifugation were collected and deposited on silicon wafers that were pre-washed with water and ethanol to remove any residues for LIBS analysis. Specifically, around 20 μl of the NP colloidal solutions (50 mg/l) were dropped casted to make the material loading densities of 1 mg/cm^2 for all the samples. All LIBS tests were carried out at ambient conditions that facilitate a simple and easy execution of the experiments.

2.3. LIBS Methodology

In this study, atomic transition lines are chosen from the NIST Atomic Energy Levels Data Center [2] (wherever available) or from other sources otherwise (as referenced) based on the relative lines strength, and transition probabilities. As Tognoni et al. [56] and Hahn et al. [22] had extensively discussed in previous LIBS studies, generally there are two quantities describing the quality of measurements in LIBS practice, signal-to-noise ratio (SNR) and peak-to-base ratio (PTB). For all samples, (i.e., PtNi, PtCo, PdCo), the optimum gate delays are determined based on the variations of the signal-to-noise ratio (SNR) as a function of gate delays for the respective elemental species to gain maximum accuracy in our results. The SNR is calculated by measuring the peak signal value at the specific wavelength of interest for a spectral line divided by the noise of the spectra. The noise is defined as the root mean square over the baseline (~ over 40 pixel) adjacent to the analyte peak. Then, the optimum signal-to-noise ratio (I_{em}) is used as the effective emission for the population density calculations of the respective atomic species based on the Boltzmann distribution:

$$I_{em} = N_i hc \frac{A_{ki}}{\lambda_{ki}} \frac{g_k}{g_i} \exp\left(-\frac{\Delta E_{ki}}{k_B T_{exc}}\right) \quad (1)$$

where I_{em} is the optimal SNR, and N_i, A_{ki},λ_{ki}, g_k, g_i are atomic number densities at the lower energy state, Einstein's transition probability, emitted wavelength, and statistical weights for the higher (k), and lower (i) energy states respectively for the specific atomic transition of interest. ΔE_{ki} is the energy difference between the k, and i states, and T_{exc} is the plasma temperature at the optimal gate delays determined for the species of interest. Boltzmann, and Planck's constant are indicated by k_B (1.38064×10^{-23} m^2 kg/ s^2 K), and h (6.62607×10^{-34} m^2 kg/s) respectively, and c (3×10^8 m/s) is the speed of light in vacuum.

Typically, plasma temperatures are calculated based on the slope of the linear fit to the Boltzmann plot of $\ln(I_{em}\lambda_{ki}/A_{ki}g_k)$ as a function of normalized upper energy level (E_k/k_B) (derived from Eq. (1)) for multiple strong lines with sufficiently widespread upper energy levels. The validity of Eq. (1), and the linear Boltzmann plot for plasma temperature calculations is based on the assumption of local thermodynamics equilibrium (LTE) conditions for the laser induced plasma. LTE requires that the plasma quenching processes are predominantly collisional rather than radiative. Typically, such conditions are established within at longer times of plasma evolution (> 1 μs) [57]. Thus, all our emission lines are measured at gate delayed beyond 1 μs. As Mukherjee et al. [23] had discussed in details, both absolute and relative emission intensities are affected by instrument uncertainty such as optical alignment, slit width etc., and the plasma fluctuations due to laser shot-to-shot variations. Moreover, the plasma temperature changes with time, and its estimation from the Boltzmann plots at different gate delays also result in the estimation of population densities being relative. Therefore, it is essential to calibrate the population densities of the analyte species of interest against those for bulk matrix species at similar plasma conditions to nullify the aforesaid plasma artifacts. To the end, the stoichiometric ratio between any two species X, and Y of interest is finally estimated through the following normalization technique:

$$R_{stoich} = \frac{[X]}{[Y]} = \frac{[N_i^{X\ I}/N_i^{B\ I}]_{@\,GD=t_1}}{[N_i^{Y\ I}/N_i^{B\ I}]_{@\,GD=t_2}} \quad (2)$$

where, N_i^X , and N_i^B represents the lower energy state population densities of the analyte X, and the bulk species respectively.

2.4. Other characterizations

In order to verify the attained results from LIBS, we used the same samples and measured the elemental ratio using ICP-OES. The NAs and NCs are digested using aqua regia solution, and diluted to be used in ICP. Standard cobalt dichloride solution (≥99%) and Na_2PdCl_4 solution (> 99.9%) are used for calibration of PdCo NA. For the PtCo NC standard cobalt dichloride solution (≥99%) and K_2PtCl_4 solution (> 99.9%), and for the PtNi NA standard nickel dichloride solution (≥99%) and and K_2PtCl_4 solution (> 99.9%) are used to calibrate the ICP with respect to the analytes of interest. Then, the standard samples and LASiS-GRR samples are both analyzed with ICP-OES (Perkin Elmer, Optima 4300 DV). Moreover, the morphology, structure and qualitative chemical composition of all the LASiS-GRR products (NAs and NCs) are analyzed with Transmission Electron Microscopy (TEM) images and Energy Dispersive X-ray Spectroscopy (EDX).

3. Results and discussion

3.1. PtNi nanoalloy analysis

Preliminary analysis for the size, structural and compositional characteristics of the PtNi NA samples synthesized via LASiS-GRR are observed from TEM and XRD measurements in Fig. 2. The TEM image in Fig. 2a reveals the largely spherical structures of the PtNi NAs with mean sizes of ~10 nm. Preliminary EDX results also confirm qualitatively that the NPs comprise Pt, and Ni as the main atomic constituents. The high-angle annular dark-field (HAADF) image and the EDX mappings (Fig. 2b-d) indicate that both Pt and Ni are uniformly distributed in the bright spherical NPs, which confirm the formation of PtNi alloy. Moreover, absence of O in Fig. 2e indicates formation of NAs as compared to the metal/metal oxide NCs. The Cu peak in EDX spectrum (Fig. 2f) for the identified spot corresponds to TEM carbon film with copper grids. The EDX spectrum also confirms that all other residual elements from the salts and other chemicals (such as K_2PtCl_4 and KCl) are washed way during the centrifugation process. Upon qualitative confirmation of the uniform distribution of Pt and Ni from our preliminary characterizations on the NA samples, the sample is drop cast on Si wafers for quantitative LIBS measurements. The atomic emission lines of Pt I (306.47 nm) and Ni I (349.29 nm) used for the population density calculations from quantitative spectral analysis are shown in Table 1. The specific choice of the lines are based on their robust transition probabilities and line strengths, while bearing in mind that their lower energy states are identified as close as possible to the ground states (i.e., E_i~0 eV) (see Table 1). Although the aforesaid Pt I and Ni I lines are listed in NIST Spectral Database [2], their detailed properties are referenced from another source [1] due to the lack of detailed information on the Pt lines from the NIST database. The temporal evolution of SNRs for the Pt I (306.47 nm), and Ni I (349.29 nm) transition lines are collected at a fixed gate width of 5 μs, as shown in Fig. 3a and b respectively. Since

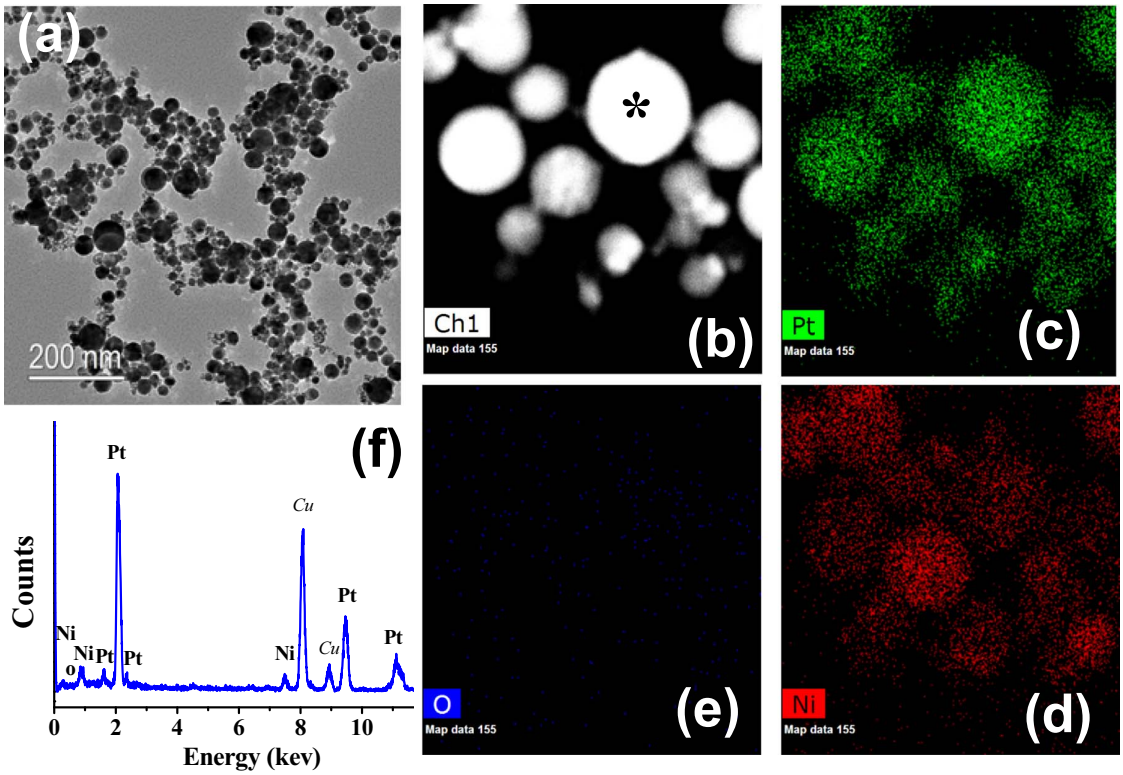

Fig. 2. (a) respective TEM image for PtNi NA/ the inset indicates the corresponding electron distribution pattern. (b) HAADF image and (c–e) EDX elemental mapping for Pt, Ni, O respectively, (f) EDX spectrum at the identified spot (*) in (b).

Table 1
Atomic spectral database [2] for Pt I and Ni I emission lines used for the population density calculations during quantitative analysis of PtNi NAs.

Species	Wavelength, λ_{ki} (nm)	Transition probability, A_{ki} (10^6 1/s)	Upper energy level, E_k (eV)	Lower energy level, E_i (eV)	g_k	g_i
Ni I	349.29	98	3.66	0.11	3	5
Pt I[a]	306.47	67	3.914	0	5	7
O I[b]	777.19	36.9	10.741	9.146	7	5

[a] From reference [1].
[b] Used for the internal calibration standard.

the Ni I (349.29 nm) emission line did not show a clear, distinct peak, a curve fit was used to obtain the optimal gate delay. From these plots, the optimal gate delays are estimated to be 3.5 μs and 5.2 μs for the respective Pt I and Ni I lines. The spectral emission lines for Pt I (306.47 nm), and Ni I (349.29 nm) are illustrated in Fig. 4a & b at the respective gate delays of 3.5 and 5.2 μs respectively. It needs to be pointed out here that the spectral window in Fig. 4a also indicate the presence of other Pt I transition lines at 292.98 nm and 299.8 nm but the 306.47 nm transition line, being the strongest and devoid of any interference from other plasma emission lines, was chosen for all our spectral analysis here. The corresponding plasma excitation temperatures (T_{exc}) needed for Pt and Ni atomic number density calculations from spectral analyses (Eq. (1) described earlier in methodology section) are estimated from the respective linear Boltzmann plots at 3.5 and 5.2 μs gate delays, shown as insets in Fig. 4a & b respectively. Here a series of Pt I lines with known robust spectral properties, as listed in Table 2, are chosen for the construction of the aforesaid linear Boltzmann plots. Based on the slopes of the Boltzmann plots (indicated in the insets in Fig. 4a & b), the plasma excitation temperatures are estimated to be 5747 ± 1889 K, and 5556 ± 2019 K at 3.5 and 5.2 μs gate delays respectively. Since our experiments are carried out in ambient conditions, the population densities of the aforesaid analyte

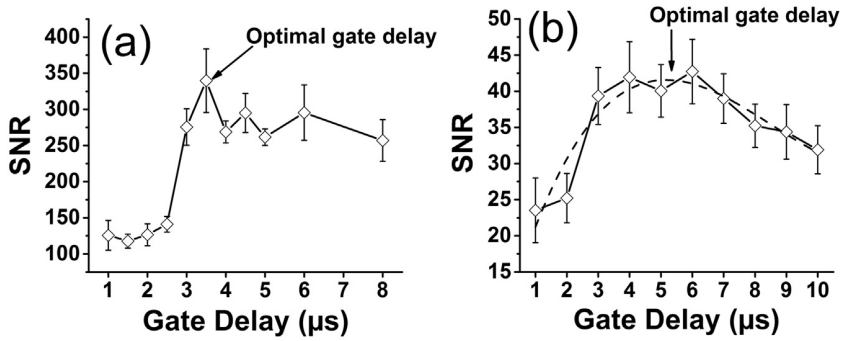

Fig. 3. Temporal evolution of signal-to-noise ratio for (a) Pt I (306.47 nm), and (b) Ni I (349.29 nm) over time. The optimal gate delays were determined to be 3.5 μs and 5.2 μs for the peak signal-to-noise ratio for Pt I (306.47 nm), and Ni I (349.29 nm) respectively.

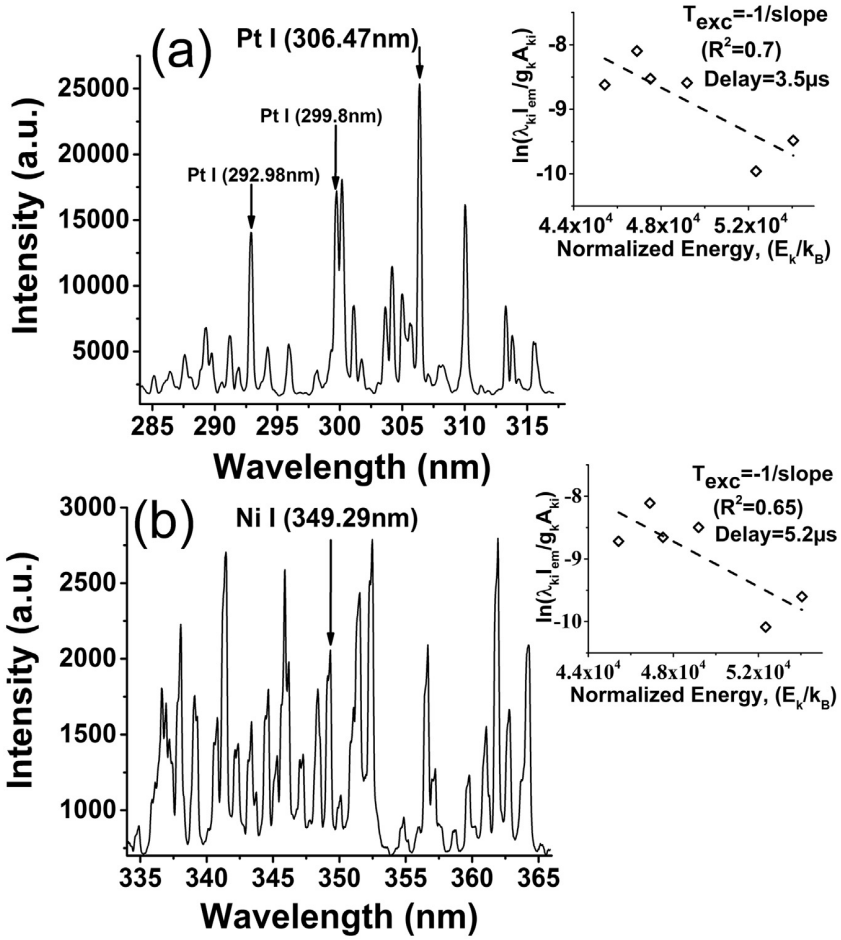

Fig. 4. Spectral emission signature for (a) Pt I (306.47 nm), and (b) Ni I (349.29 nm) lines at the respective gate delays of 3.5 μs, and 5.2 μs/ Inset shows the linear Boltzmann plots generated from Pt I lines listed in Table 2, and used for T_{exc} calculations at the respective gate delays of 3.5 μs and 5.2 μs.

Table 2
Atomic spectral database [1] for different Pt atomic emission lines used for the plasma temperature calculations at 3.5 μs, and 5.2 μs for spectral analysis of Pt Ni NAs.

Species	Wavelength, λ_{ki} (nm)	Transition probability, A_{ki} (10^6 1/s)	Upper energy level, E_k (eV)	Lower energy level, E_i (eV)	g_k	g_i
Pt I	262.803	59	4.65790896	0.09310704	5	5
Pt I	265.945	99	4.51086828	0	9	7
Pt I	283.02	24	4.23859836	0	7	7
Pt I	289.38	7.7	4.23859836	0.09310704	7	5
Pt I	292.97	22.3	4.0946598	0	7	7
Pt I	299.79	33.2	4.0946598	0.09310704	7	5
Pt I	304.26	7.7	4.04164824	0.09884136	11	9
Pt I	306.47	67	3.91440216	0	5	7

species are normalized with those of oxygen atoms estimated from the atomic emission line of O I (777.19 nm). Here, we have considered the background bulk oxygen species as the internal calibration standard as discussed in details in the LIBS methodology section earlier. Thus, using Eq. (2), the quantitative estimation for $\frac{[Pt]}{[Ni]}$ is obtained from the following normalizations of Pt and Ni atomic number densities at the respective gate delay times as indicated below:

$$R_{stoich} = \frac{[Pt]}{[Ni]} = \frac{[N_i^{Pt\ I\ (306.47nm)}/N_i^{O\ I\ (777.19nm)}]_{@GD=3.5\ \mu s}}{[N_i^{Ni\ I\ (349.29nm)}/N_i^{O\ I\ (777.19nm)}]_{@GD=5.2\ \mu s}} \quad (3)$$

Based on the aforesaid expression, the stoichiometric value is estimated to be $\frac{[Pt]}{[Ni]} \sim 4.56 \pm 0.8$. The error is calculated based on the error propagation analysis due to uncertainty in SNR, and plasma excitation temperatures (T_{exc}).

3.2. PtCo nanocomposites analysis

As before, the structure, and composition of the samples are verified first from TEM and EDX measurements in Fig. 5, with the TEM image (Fig. 5a) distinctly indicating the spherical NPs dispersed in a matrix of "sponge-shaped" nanostructures. The mean sizes of the NPs are estimated to be ~5–10 nm. Furthermore, the elemental distribution of the sample, as characterized from HAADF image (Fig. 5b) along with the EDX mappings (Fig. 5b-e), indicate the presence of Co, Pt, and O respectively for the dark field images from Fig. 5b. It confirms existence of both Pt and Co in the spherical structures, and hence the formation of PtCo NAs in the bright NPs in HAADF image (Fig. 5b). Concurrently, Co is detected within the non-spherical structures (Fig. 5d), while O is almost uniformly distributed in the entire grid of the EDX mapping (Fig. 5e). The same is also corroborated by the respective EDX spectra in Fig. 5f corresponding to the sample areas indicated as (*) and (#) in Fig. 5b. Therefore, it can be qualitatively concluded that the samples are largely composed of NCs of PtCo NAs in CoOx matrices. Further investigations on the quantitative elemental analyses of the PtCo NC samples are carried out from LIBS characterizations. The Pt I (306.47 nm) line used here for all spectral calculations is the same one as used before for the PtNi case study. The cobalt atomic transition line Co I (345.35 nm) is chosen based on the transition probability and line strength as reported in details in Table 3[2]. In this case, the temporal evolution plots for SNRs

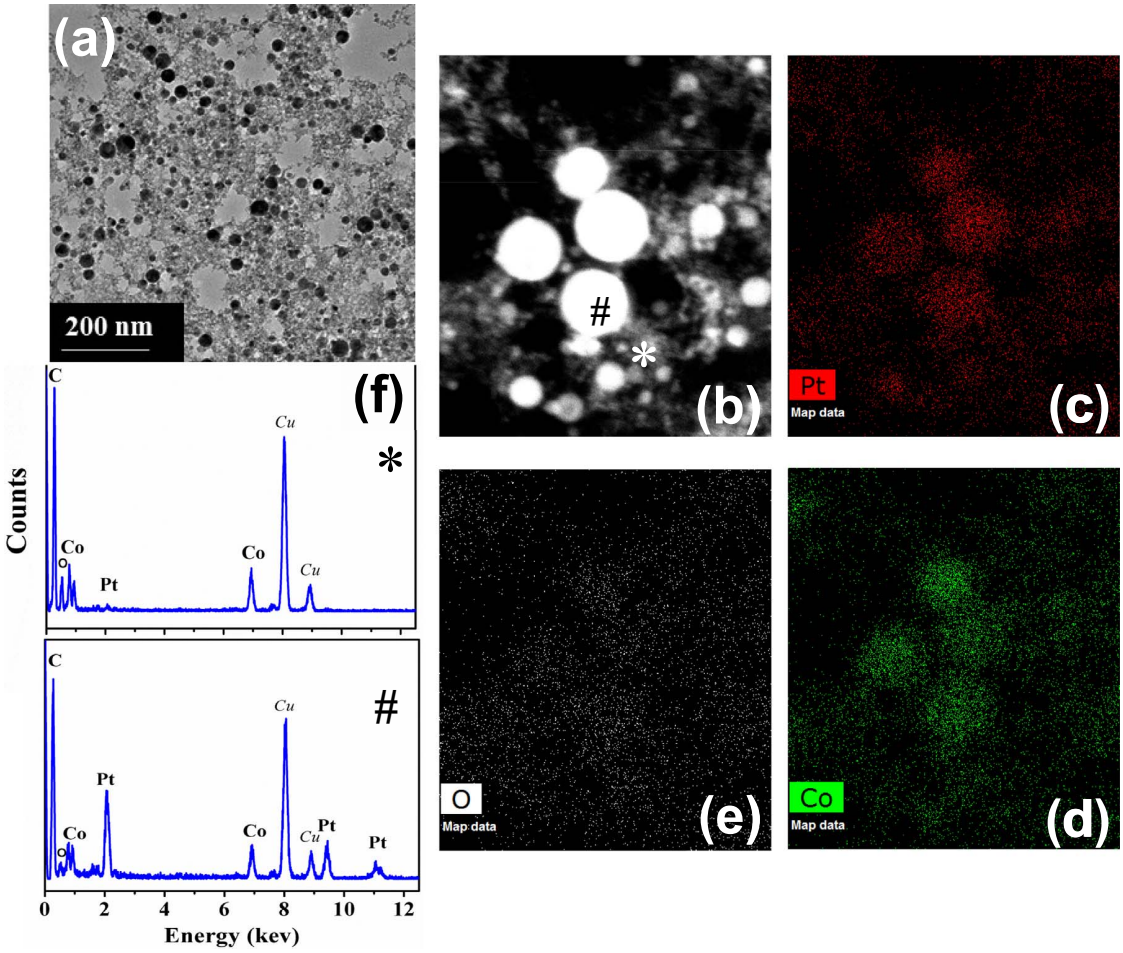

Fig. 5. (a) respective TEM image for PtCo NC, (b) HAADF image and (c-e) EDX elemental mapping for Pt, Co, O respectively, (f) EDX spectra at the respective spots identified as (*) and (#) in (b).

Table 3
Atomic spectral database [2] for Pt I and Co I emission lines used for the population density calculations during quantitative analysis of PtCo NCs.

Species	Wavelength, λ_{ki} (nm)	Transition probability, A_{ki} (10^6 1/s)	Upper energy level, E_k (eV)	Lower energy level, E_i (eV)	g_k	g_i
Co I	345.35	110	4.026	0.432	12	10
Pt I[a]	306.47	67	3.914	0	5	7

[a] From reference [1].

in Fig. 6 indicate that for both Pt I (306.47 nm) and Co I (345.35 nm) lines, the optimal gate delays appear at 4 μs for the fixed gate width of ~ 5 μs. To establish the accuracy and robustness of the quantitative LIBS technique, three different samples with varying stoichiometric compositions of PtCo NCs (PtCo1, PtCo2, and PtCo3 as prepared using the LASiS-GRR technique, and described earlier in the experimental details section) are analyzed here. Fig. 7 illustrates the characteristic emission spectra of Pt I (306.47 nm), and Co I (345.35 nm) at 4 μs gate delay at different emission windows, which reveals other emission lines of both Pt and Co at the corresponding windows. Both Pt I (306.47 nm) and Co I (345.35 nm) indicate the highest intensity values, as it was expected due to their greater transition probabilities, and emission

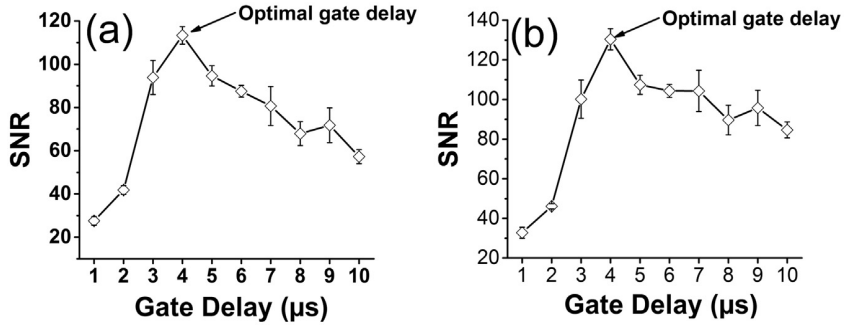

Fig. 6. Temporal evolution of signal-to-noise ratio for (a) Pt I (306.47 nm), and (b) Co I (345.35 nm) over time. The optimal gate delays were determined to be 4 μs for both Pt I (306.47 nm) and Co I (345.35 nm) for the peak signal-to-noise ratio for Pt I (306.47 nm), and Co I (345.35 nm) respectively.

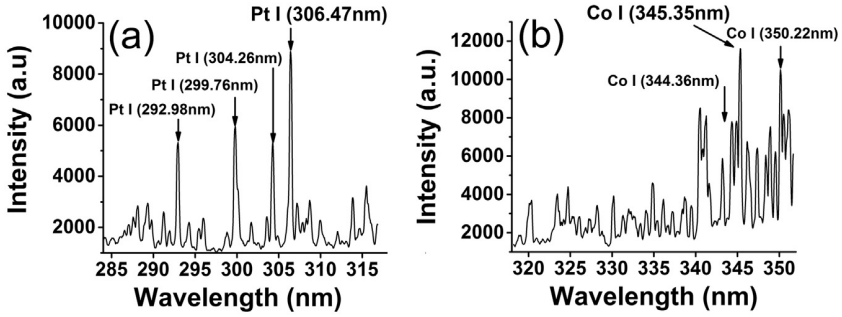

Fig. 7. Spectral emission signature for (a) Pt I (306.47 nm), and (b) Co I (345.35 nm) lines at the respective gate delays of 4 μs.

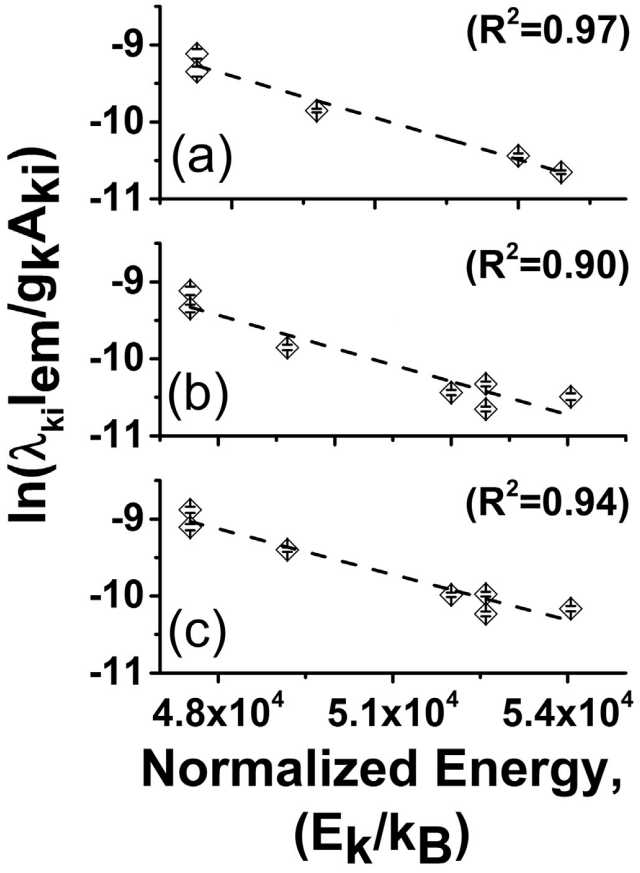

Fig. 8. Boltzmann plots for plasma temperature estimation based on the Pt I lines. (a) PtCo1 with plasma temperature 3682 ± 357 K, (b) PtCo2 with plasma temperature 4645 ± 685 K, and (c) PtCo3 with plasma temperature 5061 ± 559 K.

strengths The plasma temperatures at 4 μs gate delay times are estimated based on a linear fit to the Boltzmann plot generated from the same series of Pt I emission lines as reported earlier in Table 2. Fig. 8a-c indicates the corresponding Boltzmann plots along with the respective linear fits for the three different samples (PtCo1, PtCo2, PtCo3 respectively) under study here. The plasma temperatures (T_{exc}, K) for the three samples, as estimated from the slopes of the linear fits in Fig. 8a-c, are found to be 3682 ± 357 K (PtCo1), 4645 ± 685 K (PtCo2), and 5061 ± 559 K (PtCo3) at 4 μs gate delay times. It should be noted here that since the optimum gate delays for both Pt I (306.47 nm), and Co I (345.35 nm) occur at 4 μs, we could not use the same atomic density of bulk oxygen for normalizing the population densities of both Pt and Co as they would simply cancel each other out. Therefore, we had to resort to a similar technique employed earlier by Mukherjee et al. [29] in employing a series of different transition lines

Table 4
Atomic spectral database [2] for different Pt atomic emission lines used for the plasma temperature calculations at 4 μs and internal calibration standard, and different Co emission lines used for the internal calibration standard at 4 μs.

Species	Wavelength, λ_{ki} (nm)	Transition probability, A_{ki} (10^6 1/s)	Upper energy level, E_k (eV)	Lower energy level, E_i (eV)	g_k	g_i
Pt I[a]	262.803	59	4.65790896	0.09310704	5	5
Pt I[a]	265.945	99	4.51086828	0	9	7
Pt I[a]	283.02	24	4.23859836	0	7	7
Pt I[a]	289.38	7.7	4.23859836	0.09310704	7	5
Pt I[a]	292.97	22.3	4.0946598	0	7	7
Pt I[a]	299.79	33.2	4.0946598	0.09310704	7	5
Pt I[a]	304.26	7.7	4.04164824	0.09884136	11	9
Pt I[a]	306.47	67	3.91440216	0	5	7
Pt I[a]	330.185	25.3	4.4213652	0.78809532	3	5
Co I	340.512	100	4.071888	0.431815	10	10
Co I	344.36	69	4.112972	0.513624	8	8
Co I	345.35	110	4.020881	0.431815	12	10
Co I	350.228	80	3.970904	0.431815	8	10

[a] From reference [1].

of the analyte species itself as the internal calibrator for the normalization process. Table 4 lists all the Pt and Co lines used for the aforesaid normalization. In line with our earlier calculations, the estimated quantitative stoichiometric ratio of $\frac{[Pt]}{[Co]}$ is obtained as:

$$R_{stoich} = \frac{[Pt]}{[Co]} = \frac{[N_i^{Pt\ I\ (306.47nm)}/N_i^{Pt\ I}]_{@GD=4\mu s}}{[N_i^{Co\ I\ (345.35nm)}/N_i^{Co\ I}]_{@GD=4\mu s}} \quad (4)$$

In this case, the estimated $\frac{[Pt]}{[Co]}$ ratios for the samples are found to be: 1.13 ± 0.14 (PtCo1), 1.29 ± 0.19 (PtCo2), and 1.19 ± 0.14 (PtCo3). The uncertainties in SNRs, and plasma temperatures (T_{exc}) are considered for the error propagations here.

3.3. PdCo nanoalloy analysis

Finally, we also extended the aforesaid LIBS technique for investigating palladium cobalt (PdCo) nanoalloys synthesized via the LASiS-GRR process. The TEM and EDX measurements once again indicate the samples to comprise spherical NPs with mean sizes ~5–10 nm (TEM image in Fig. 9a), while the HAADF image in Fig. 9b along with EDX mappings for Pd, Co, O indicate that the NPs are mainly composed of Pd (Fig. 9c) with a very low atomic density of Co. Moreover, unlike the PtCo NCs reported earlier, an extremely low O distribution here confirms the formation of NAs in this case (Fig. 9e). The almost negligible O peak in EDX spectra also corroborates the same, while the relatively low Co peak (Fig. 9f), as compared to the Pd peak, qualitatively indicate the low Co to Pd ratios in the PdCo NAs. For the detailed quantitative LIBS analysis, we chose the same Co atomic transition line of Co I (345.35 nm) [2] as also used in our earlier case study of PtCo NAs. On the other hand, the Pd I (360.95 nm) [2] line chosen for the population density analysis is based on the transition

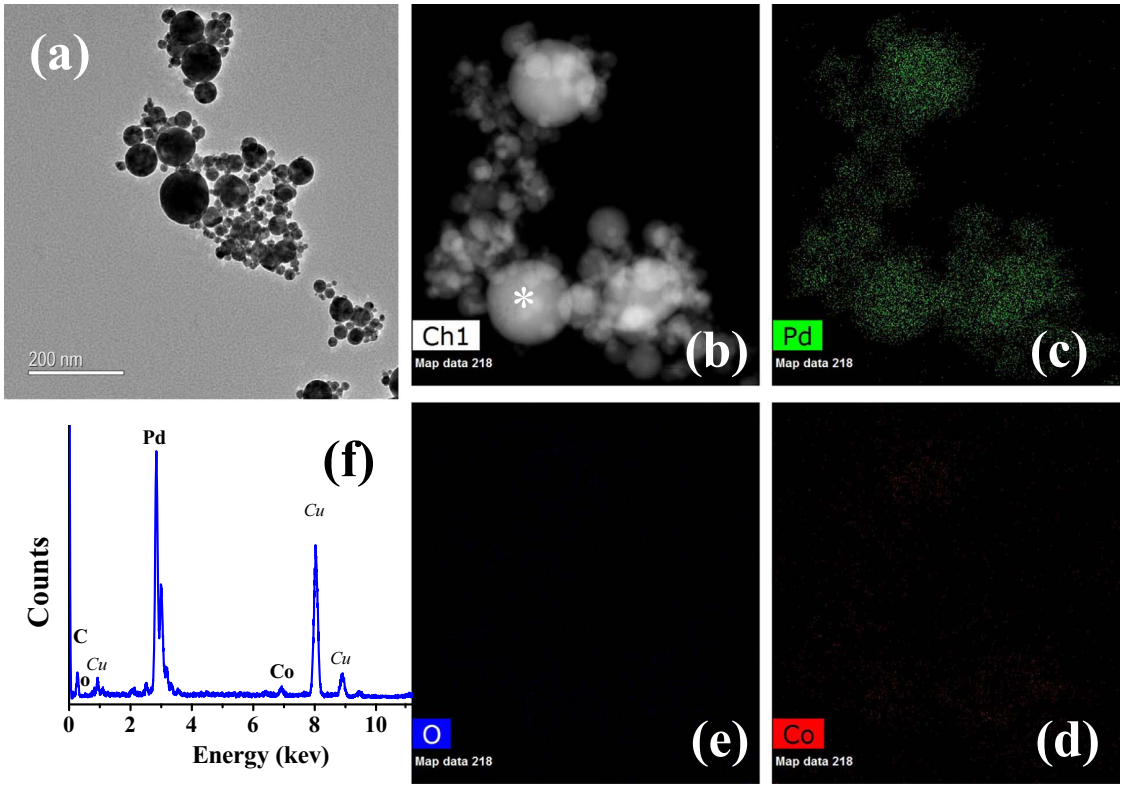

Fig. 9. (a) respective TEM image for PdCo NA, (b) HAADF image and (c–e) EDX elemental mapping for Pd, Co, O respectively, (f) EDX spectrum at the identified spot (*) in (b).

Table 5
Atomic spectral database [2] for Pd I and Co I emission lines used for the population density calculations during quantitative analysis of PdCo NAs.

Species	Wavelength, λ_{ki} (nm)	Transition probability, A_{ki} (10^6 1/s)	Upper energy level, E_k (eV)	Lower energy level, E_i (eV)	g_k	g_i
Pd I	360.95	82	4.395	0.961	7	5
Co I	345.35	110	4.026	0.432	12	10

probability and line strength as listed in Table 5. In this case, the optimal gate delay values for Pd I (360.95 nm), and Co I (345.35 nm) transition lines, determined from temporal evolution of their respective SNRs, are estimated to be 3 μs, and 7 μs for a fixed gate delay of 5 μs (as indicated Fig. 10a & b). As seen from Fig. 11a & b, both Pd I and Co I lines in this case provide the added advantage of being situated in the same spectral window. But, as expected here, the LIBS emission lines for Pd I (360.95 nm) at both 3 and 7 μs gate delay times indicate a much stronger spectral signature as compared to those for Co (see Fig. 11a & b). This clearly indicates the elemental concentration of Pd to be significantly higher than that for Co in the as-synthesized PdCo NAs. It is worth mentioning that although the Co I (345.35 nm) absolute emission intensity at 3 μs is slightly higher than the corresponding value at 7 μs, the SNR is significantly lower due to the higher background noise at earlier delay times. In the choice of emission lines of the analyte species themselves for the normalization process in this case, we had to judiciously use different Pd I lines only due to the weak signatures of the Co I lines. It should also be noted here that the rapid disappearance of oxygen emission lines, O I (777.19 nm) at later delay times made it not possible for us to use atomic densities as estimated from O I (777.19 nm) line at 7 μs gate delay time for the normalization process. Thus, Table 6 lists all the Pd I atomic transition lines used for the normalization technique here. The identification of a series of strong Pd I emission lines, as listed in Table 6, also enabled us to use the same lines for plasma temperature calculations from the linear Boltzmann plots (as described earlier) at the respective delay times of 3 μs and 7 μs. The corresponding plasma temperatures are reported to

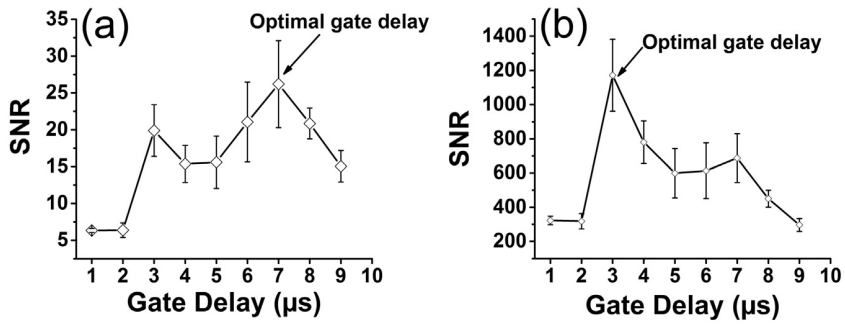

Fig. 10. Temporal evolution of signal-to-noise ratio for (a) Co I (345.35 nm), and (b) Pd I (360.95 nm) over time. The optimal gate delays were determined to be 3 μs and 7 μs for the peak signal-to-noise ratio for Pd I (360.95 nm), and Co I (345.35 nm) respectively.

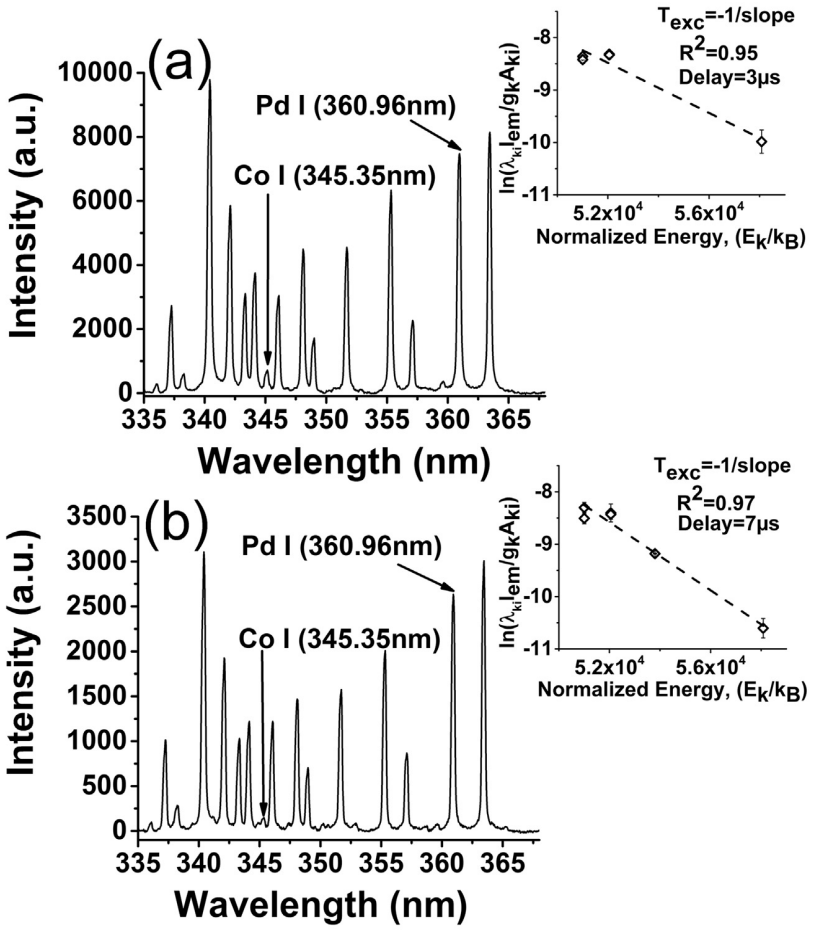

Fig. 11. Spectral emission signature for Pd I (360.59 nm), and Co I (345.35 nm) lines at (a) 3 μs, and (b) 7 μs gate delays / Inset shows the linear Boltzmann plots generated from Pd I lines listed in Table 6, and used for T_{exc} calculations at the respective gate delays of 3 μs and 7 μs.

Table 6
Atomic spectral database [2] for Pd atomic emission lines used for plasma temperature calculations and internal calibrations at 3 μs, 7 μs for spectral analysis of PdCo NAs.

Species	Wavelength, λ_{ki} (nm)	Transition probability, A_{ki} (10^6 1/s)	Upper energy level, E_k (eV)	Lower energy level, E_i (eV)	g_k	g_i
Pd I	247.64	11.8	5.0050928	0	3	1
Pd I	276.31	16.9	4.4858322	0	3	1
Pd I	324.26	77	4.6362356	0.8138506	7	7
Pd I	346.07	30	4.3954187	0.8138506	7	7
Pd I	351.69	103	4.4858322	0.9615006	3	5
Pd I	360.95	820	4.3954187	0.9615006	7	5

be 4184 ± 554 K, and 3076 ± 285 K respectively. Finally, similar to the methodology explained earlier, the estimated quantitative stoichiometric ratio of $\frac{[Co]}{[Pd]}$ is obtained as:

$$R_{stoich} = \frac{[Co]}{[Pd]} = \frac{[N_i^{Co\ I\ (345.35nm)}/N_i^{Pd\ I}]_{@GD=3\mu s}}{[N_i^{Pd\ I\ (360.95nm)}/N_i^{Pd\ I}]_{@GD=7\mu s}} \quad (5)$$

The estimated stoichiometric ratio for PdCo nanoalloys is 0.06 ± 0.005. The low amount of cobalt in the nanoalloy is in agreement with the EDX results, which had also qualitatively indicated a low distribution of cobalt in the nanoalloy. Furthermore, the results in this case demonstrate the resolution of our quantitative LIBS methodology in estimating trace level elemental ratios in alloyed nanoparticles.

3.4. Comparison with ICP-OES

In this section, we verify our current LIBS results for the quantitative elemental ratios of the NA/NC samples studied here by comparing against the corresponding results obtained from standard ICP-OES measurements. To this end, Table 7 lists the comparisons between values for the elemental ratios of PtNi, PtCo1, PtCo2, PtCo3 and PdCo samples as obtained from LIBS and ICP-OES analyses. For ease of comparison and understanding, Fig. 12 plots the LIBS results for the aforesaid estimated elemental stoichiometric ratios against those obtained from ICP measurements. Here, the black dashed line represents the ideal one-to-one correlation between the LIBS and ICP-OES results. As can be observed from Fig. 12, the LIBS results are in good agreement with the values predicted from ICP-OES results. It needs to be highlighted here that we purposely chose to work with intermetallic nanomaterials that were synthesized with widely varying elemental ratios (~0.04-6.00) in order to test the robustness and accuracy of the

Table 7
Comparison of the quantitative elemental ratios, as estimated from LIBS and ICP-OES measurements, for the different NAs and NCs under study.

Sample	PtNi	PtCo1	PtCo2	PtCo3	PdCo
Elemental ratio	$\frac{[Pt]}{[Ni]}$	$\frac{[Pt]}{[Co]}\Big\vert_{PtCo\ 1}$	$\frac{[Pt]}{[Co]}\Big\vert_{PtCo\ 2}$	$\frac{[Pt]}{[Co]}\Big\vert_{PtCo\ 3}$	$\frac{[Co]}{[Pd]}$
LIBS	4.55	1.13	1.29	1.19	0.06
ICP-OES	5.16	0.71	1.03	1.35	0.04

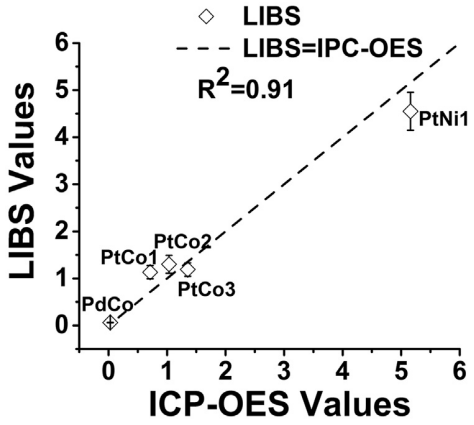

Fig. 12. Comparison between LIBS, and ICP results. The line represents the ideal agreement between two instruments.

quantitative LIBS analysis for characterizing NPs with a wide range of intermetallic compositions. The error bars in the LIBS have been calculated based on the error propagations due to uncertainties in plasma temperatures (T_{exc}), and shot-to-shot variations in the laser-induced plasma. It is worth mentioning that the samples with larger standard experimental errors indicated larger uncertainties. However, the relative standard errors remained almost the same for the various samples with different elemental ratios. In regards to the slight variations in the LIBS results from the ICP-OES measurements as observed from Table 7 in some of the cases, one needs to bear in mind that the accuracy of quantitative LIBS analysis has an exponential dependence on the calculated plasma temperatures. Furthermore, self-absorptions can also affect the collected emission intensities and consequently the calculated temperatures. To this end, typically purging neutral gases such as argon and specially helium can thin the plasma considerably thereby reducing the self-absorption effects. However, our focus in the current study being on establishing the robustness and relative accuracy of LIBS for rapid and facile quantitative characterizations of intermetallic NPs, all our experiments were carried out under ambient conditions. Thus, considering the minimal sample preparation steps along with the simplicity and rapidity of quantitative spectral analysis offered by LIBS, the deviations of our current results are satisfactory.

4. Conclusion

In this study, we demonstrate the application of LIBS for quantitative chemical characterizations of intermetallic nanoalloys (NAs), and nanocomposites (NCs) with sizes $< 10 - 15$ nm synthesized as electrocatalysts via our in-house developed laser ablation technique (LASiS-GRR). We employ an internal calibration methodology that involves effective normalizations of the analyte species densities by bulk species densities, both estimated from atomic emission lines at identical laser-induced plasma conditions, to carry out quantitative spectral analysis without the need for any external standards. The results from LIBS are in good agreement with those measured from ICP-OES. The minimal sample preparations and rapid measurement capabilities of LIBS, as compared to the time consuming steps and extensive acid digestion procedures involved with ICP-OES measurements, make it an ideal candidate for quantitative spectrochemical analysis of heterogeneous nanomaterials. Specifically, our results establish the promising potential of LIBS as the future analytical technique of choice for facile and rapid screening of intermetallic nanocatalysts designed with tailored structures and compositions.

References

[1] E.A. Den Hartog, M.T. Herd, J.E. Lawler, C. Sneden, J.J. Cowan, T.C. Beers, Improved laboratory transition probabilities for PtI and application to the platinum abundances of BD+17 degrees 3248 and the Sun, Astrophys. J. 619 (1) (2005) 639–655.
[2] A. Kramida, Y. Ralchenko, J. Reader, NIST ASD Team, NIST Atomic Spectra Database (version 5.3). [[Online]] ⟨http://physics.nist.gov/asd⟩, 2015
[3] P.F. Zhang, X.P. Dai, X. Zhang, et al., One-pot synthesis of ternary pt-ni-cu nanocrystals with high catalytic performance, Chem. Mater. 27 (18) (2015) 6402–6410.
[4] J. Luo, L.Y. Wang, D. Mott, et al., Ternary alloy nanoparticles with controllable sizes and composition and electrocatalytic activity, J. Mater. Chem. 16 (17) (2006) 1665–1673.
[5] H.Y. Zhu, S. Zhang, S.J. Guo, D. Su, S.H. Sun, Synthetic control of FePtM nanorods (M = Cu, Ni) to enhance the oxygen reduction reaction, J. Am. Chem. Soc. 135 (19) (2013) 7130–7133.
[6] S. Hu, M. Tian, E.L. Ribeiro, G. Duscher, D. Mukherjee, Tandem laser ablation synthesis in solution-galvanic replacement reaction (LASiS-GRR) for the production of PtCo nanoalloys as oxygen reduction electrocatalysts, J. Power Sources 306 (2016) 413–423.
[7] M.E. Scofield, C. Koenigsmann, L. Wang, H. Liu, S.S. Wong, Tailoring the composition of ultrathin, ternary alloy PtRuFe nanowires for the methanol oxidation reaction and formic acid oxidation reaction, Energy Environ. Sci. 8 (1) (2015) 350–363.
[8] M.A. Matin, E. Lee, H. Kim, W.-S. Yoon, Y.-U. Kwon, Rational syntheses of core-shell Fe@(PtRu) nanoparticle electrocatalysts for the methanol oxidation reaction with complete suppression of CO-poisoning and highly enhanced activity, J. Mater. Chem. A 3 (33) (2015) 17154–17164.
[9] D.-Y. Wang, H.-L. Chou, Y.-C. Lin, et al., Simple replacement reaction for the preparation of ternary fe1-xptrux nanocrystals with superior catalytic activity in methanol oxidation reaction, J. Am. Chem. Soc. 134 (24) (2012) 10011–10020.
[10] S. Hu, G. Goenaga, C. Melton, T.A. Zawodzinski, D. Mukherjee, PtCo/CoOx nanocomposites: bifunctional electrocatalysts for oxygen reduction and evolution reactions synthesized via tandem laser ablation synthesis in solution-galvanic replacement reactions, Appl. Catal. B: Environ. 182 (2016) 286–296.
[11] Y. Zhu, C. Su, X. Xu, W. Zhou, R. Ran, Z. Shao, A universal and facile way for the development of superior bifunctional electrocatalysts for oxygen reduction and evolution reactions utilizing the synergistic effect, Chem. (Weinh. der Bergstr. Ger.) 20 (2014) 15533–15542.
[12] Y.J. Sa, K. Kwon, J.Y. Cheon, F. Kleitz, S.H. Joo, Ordered mesoporous Co3O4 spinels as stable, bifunctional, noble metal-free oxygen electrocatalysts, J. Mater. Chem. A. 1 (2013) 9992.
[13] Y. Gorlin, T.F. Jaramillo, A bifunctional nonprecious metal catalyst for oxygen reduction and water oxidation, J. Am. Chem. Soc. 132 (39) (2010) 13612–13614.
[14] S. Koh, M.F. Toney, P. Strasser, Activity-stability relationships of ordered and disordered alloy phases of Pt3Co electrocatalysts for the oxygen reduction reaction (ORR), Electrochim. Acta 52 (8) (2007) 2765–2774.
[15] D.L. Wang, H.L.L. Xin, R. Hovden, et al., Structurally ordered intermetallic platinum-cobalt core-shell nanoparticles with enhanced activity and stability as oxygen reduction electrocatalysts, Nat. Mater. 12 (1) (2013) 81–87.
[16] B.J. Hwang, S.M.S. Kumar, C.H. Chen, et al., An investigation of structure-catalytic activity relationship for Pt-Co/C bimetallic nanoparticles toward the oxygen reduction reaction, J. Phys. Chem. C. 111 (42) (2007) 15267–15276.
[17] S.C. Zignani, E. Antolini, E.R. Gonzalez, Evaluation of the stability and durability of Pt and Pt-Co/C catalysts for polymer electrolyte membrane fuel cells, J. Power Sources 182 (1) (2008) 83–90.
[18] M. Tighe, P. Lockwood, S. Wilson, L. Lisle, Comparison of digestion methods for ICP-OES analysis of a wide range of analytes in heavy metal contaminated soil samples with specific reference to arsenic and antimony, Commun. Soil Sci. Plan. 35 (9–10) (2004) 1369–1385.
[19] O.V. Borisov, D.M. Coleman, K.A. Oudsema, R.O. Carter, Determination of platinum, palladium, rhodium and titanium in automotive catalytic converters using inductively coupled plasma mass spectrometry with liquid nebulization, J. Anal. At. Spectrom. 12 (2) (1997) 239–246.
[20] M.C.E. Lomer, R.P.H. Thompson, J. Commisso, C.L. Keen, J.J. Powell, Determination of titanium dioxide in foods using inductively coupled plasma optical emission spectrometry, Analyst 125 (12) (2000) 2339–2343.
[21] L.J. Radziemski, D.A. Cremers, Spectrochemical analysis using laser plasma excitation, in: L.J. Radziemski, D.A. Cremers (Eds.), Laser-Induced Plasmas and Applications, New York: Marcel Dekker Inc, 1989, pp. 6107–6118.
[22] D.W. Hahn, N. Omenetto, Laser-Induced Breakdown Spectroscopy (LIBS), Part II: review of instrumental and methodological approaches to material analysis and applications to different fields, Appl. Spectrosc. 66 (4) (2012) 347–419.
[23] D. Mukherjee, A. Rai, M.R. Zachariah, Quantitative laser-induced breakdown spectroscopy for aerosols via internal calibration: application to the oxidative coating of aluminum nanoparticles, J. Aerosol Sci. 37 (6) (2006) 677–695.
[24] F. Ferioli, S.G. Buckley, Measurements of hydrocarbons using laser-induced breakdown spectroscopy, Combust. Flame 144 (3) (2006) 435–447.
[25] A.E. Majd, A.S. Arabanian, R. Massudi, M. Nazeri, Spatially resolved laser-induced breakdown spectroscopy in methane-air diffusion flames, Appl. Spectrosc. 65 (1) (2011) 36–42.
[26] F. Ferioli, P.V. Puzinauskas, S.G. Buckley, Laser-induced breakdown spectroscopy for on-line engine equivalence ratio measurements, Appl. Spectrosc. 57 (9) (2003) 1183–1189.

[27] R. Wisbrun, I. Schechter, R. Niessner, H. Schroder, K.L. Kompa, Detector for trace elemental analysis of solid environmental-samples by laser-plasma spectroscopy, Anal. Chem. 66 (18) (1994) 2964–2975.
[28] D.A. Cremers, M.H. Ebinger, D.D. Breshears, et al., Measuring total soil carbon with laser-induced breakdown spectroscopy (LIBS), J. Environ. Qual. 30 (6) (2001) 2202–2206.
[29] D. Mukherjee, M.D. Cheng, Quantitative analysis of carbonaceous aerosols using laser-induced breakdown spectroscopy: a study on mass loading induced plasma matrix effects, J. Anal. At. Spectrom. 23 (1) (2008) 119–128.
[30] J.L. Gottfried, Discrimination of biological and chemical threat simulants in residue mixtures on multiple substrates, Anal. Bioanal. Chem. 400 (10) (2011) 3289–3301.
[31] J.L. Gottfried, F.C. De Lucia, C.A. Munson, A.W. Miziolek, Standoff detection of chemical and biological threats using laser-induced breakdown spectroscopy, Appl. Spectrosc. 62 (4) (2008) 353–363.
[32] B.E. Naes, S. Umpierrez, S. Ryland, C. Barnett, J.R. Almirall, A comparison of laser ablation inductively coupled plasma mass spectrometry, micro X-ray fluorescence spectroscopy, and laser induced breakdown spectroscopy for the discrimination of automotive glass, Spectrochim. Acta B 63 (10) (2008) 1145–1150.
[33] J.L. Gottfried, Influence of metal substrates on the detection of explosive residues with laser-induced breakdown spectroscopy, Appl Opt. 52 (4) (2013) B10–B19.
[34] F.C. De Lucia, J.L. Gottfried, Influence of molecular structure on the laser-induced plasma emission of the explosive rdx and organic polymers, J. Phys. Chem. A 117 (39) (2013) 9555–9563.
[35] J.L. Gottfried, F.C. De Lucia, C.A. Munson, A.W. Miziolek, Laser-induced breakdown spectroscopy for detection of explosives residues: a review of recent advances, challenges, and future prospects, Anal. Bioanal. Chem. 395 (2) (2009) 283–300.
[36] D. Mukherjee, M.D. Cheng, Characterization of carbon-containing aerosolized drugs using laser-induced breakdown spectroscopy, Appl. Spectrosc. 62 (5) (2008) 554–562.
[37] L. St-Onge, E. Kwong, M. Sabsabi, E.B. Vadas, Quantitative analysis of pharmaceutical products by laser-induced breakdown spectroscopy, Spectrochim. Acta B 57 (7) (2002) 1131–1140.
[38] A. Kumar, F.Y. Yueh, J.P. Singh, S. Burgess, Characterization of malignant tissue cells by laser-induced breakdown spectroscopy, Appl Opt. 43 (28) (2004) 5399–5403.
[39] V.K. Singh, A.K. Rai, Potential of laser-induced breakdown spectroscopy for the rapid identification of carious teeth, Laser Med. Sci. 26 (3) (2011) 307–315.
[40] R. Sattmann, V. Sturm, R. Noll, Laser-Induced breakdown spectroscopy of steel samples using multiple Q-switch Nd-Yag laser-pulses, J. Phys. D Appl. Phys. 28 (10) (1995) 2181–2187.
[41] D.E. Kim, K.J. Yoo, H.K. Park, K.J. Oh, D.W. Kim, Quantitative analysis of aluminum impurities in zinc alloy by laser-induced breakdown spectroscopy, Appl. Spectrosc. 51 (1) (1997) 22–29.
[42] J.M. Li, L.B. Guo, N. Zhao, et al., Determination of cobalt in low-alloy steels using laser-induced breakdown spectroscopy combined with laser-induced fluorescence, Talanta 151 (2016) 234–238.
[43] D.W. Hahn, Laser-induced breakdown spectroscopy for sizing and elemental analysis of discrete aerosol particles, Appl. Phys. Lett. 72 (23) (1998) 2960–2962.
[44] D.W. Hahn, M.M. Lunden, Detection and analysis of aerosol particles by laser-induced breakdown spectroscopy, Aerosol Sci. Technol. 33 (1–2) (2000) 30–48.
[45] J.E. Carranza, D.W. Hahn, Assessment of the upper particle size limit for quantitative analysis of aerosols using laser-induced breakdown spectroscopy, Anal. Chem. 74 (21) (2002) 5450–5454.
[46] A. Kebede, A.K. Singh, P.K. Rai, et al., Controlled synthesis, characterization, and application of iron oxide nanoparticles for oral delivery of insulin, Laser Med. Sci. 28 (2) (2013) 579–587.
[47] T. Stehrer, B. Praher, R. Viskup, et al., Laser-induced breakdown spectroscopy of iron oxide powder, J. Anal. At. Spectrom. 24 (7) (2009) 973–978.
[48] Y.Y. Zhang, S.Q. Li, Y.H. Ren, Q. Yao, S.D. Tse, A new diagnostic for volume fraction measurement of metal-oxide nanoparticles in flames using phase-selective laser-induced breakdown spectroscopy, Proc. Combust. Inst. 35 (2015) 3681–3688.
[49] J. Serrano, L. Cabalín, J. Moros, J. Laserna, Potential of laser-induced breakdown spectroscopy for discrimination of nano-sized carbon materials. Insights on the optical characterization of graphene, Spectrochim. Acta Part B: At. Spectrosc. 97 (2014) 105–112.
[50] S. Petrovic, B. Salatic, D. Milovanovic, et al., Agglomeration in core-shell structure of CuAg nanoparticles synthesized by the laser ablation of Cu target in aqueous solutions, J. Opt.-Uk 17 (2) (2015).
[51] K. Kadel, W.Z. Li, Solvothermal synthesis and structural characterization of unfilled and Yb-filled cobalt antimony skutterudite, Cryst. Res. Technol. 49 (2–3) (2014) 135–141.
[52] A. Ciucci, M. Corsi, V. Palleschi, S. Rastelli, A. Salvetti, E. Tognoni, New procedure for quantitative elemental analysis by laser-induced plasma spectroscopy, Appl. Spectrosc. 53 (8) (1999) 960–964.
[53] L.X. Sun, H.B. Yu, Correction of self-absorption effect in calibration-free laser-induced breakdown spectroscopy by an internal reference method, Talanta 79 (2) (2009) 388–395.
[54] E. Tognoni, G. Cristoforetti, S. Legnaioli, V. Palleschi, Calibration-Free Laser-Induced Breakdown Spectroscopy: state of the art, Spectrochim. Acta B 65 (1) (2010) 1–14.
[55] S. Hu, C. Melton, D. Mukherjee, A facile route for the synthesis of nanostructured oxides and hydroxides of cobalt using laser ablation synthesis in solution (LASIS), Phys. Chem. Chem. Phys. 16 (43) (2014) 24034–24044.
[56] E. Tognoni, G. Cristoforetti, [INVITED] Signal and noise in Laser Induced Breakdown Spectroscopy: an introductory review, Opt. Laser Technol. 79 (2016) 164–172.
[57] L.J. Radziemski, T.R. Loree, D.A. Cremers, N.M. Hoffman, Time-resolved laser-induced breakdown spectrometry of aerosols, Anal. Chem. 55 (8) (1983) iso#2008.